Corrosion Science 161 (2019) 108198

Contents lists available at ScienceDirect

Corrosion Science

journal homepage: www.elsevier.com/locate/corsci

Reduction of austenite-ferrite galvanic activity in the heat-affected zone of a Gleeble-simulated grade 2205 duplex stainless steel weld

P. Reccagni[a], L.H. Guilherme[b], Q. Lu[c], M.F. Gittos[c], D.L. Engelberg[a,*]

[a] Corrosion and Protection Centre, University of Manchester, UK
[b] Engineering Department, Soudap Engineering Company, Araraquara, SP, Brazil
[c] TWI, Cambridge, UK

ARTICLE INFO

Keywords:
A. Duplex stainless steel, Gleeble
B. SKPFM, polarization
C. Welding, passive film

ABSTRACT

A Gleeble-simulated microstructure of the heat-affected zone (HAZ) of tungsten inert gas (TIG) welded grade 2205 duplex stainless steel (DSS) has been produced. Local changes in microstructure chemistry were correlated to galvanic activity using scanning Kelvin probe force microscopy (SKPFM) and electro-chemical polarization. The simulated HAZ had a marked reduction of SKPFM measured Volta potentials. This was reflected in a clear reduction of the electrochemical potential difference of the activation peak between the ferrite and austenite phase. The implications of these observations are discussed for reducing the likelihood of environmentally assisted cracking.

1. Introduction

Duplex stainless steels (DSSs) have been increasingly used in the energy and chemical industries due to their excellent combination of mechanical strength and corrosion resistance, with far superior stress corrosion cracking (SCC) performance in chloride-containing environments than comparable austenitic grades [1–3]. The properties of DSSs rely on a microstructure with equal proportions of γ-austenite (face centred cubic, FCC) and δ-ferrite (body centred cubic, BCC) [4]. The partitioning of austenite-forming (Ni, N) and ferrite-forming (Cr, Mo) elements results in different chemical compositions and corrosion properties for the two phases [5,6]. The consequent galvanic activity between austenite and ferrite is recognised as a key property for the SCC resistance of DSSs, with the ferrite cathodically protecting the austenite in acidic, chloride-containing environments [7].

Arc welding is widely used to join and fabricate structures via fusion welding processes [8]. As a consequence of the welding process, the heat-affected zone (HAZ) surrounding DSSs welds normally shows an increased ferrite fraction and the compositions of the two phases are modified with respect to those in the base metal [9,10]. Due to the microstructural changes, this region of the weld shows increased susceptibility to localised corrosion and SCC [11]. Even when an acceptable phase balance is achieved and third phase (e.g. σ-sigma, χ-chi, Cr-Nitrides) precipitation is avoided [9,12], a better understanding of the SCC susceptibility in the HAZ is required [13].

The effect of welding on the austenite-ferrite galvanic activity in the HAZ is investigated in this work. A microstructure representative of an HAZ was produced using thermo-mechanical simulation and the HAZ microstructure was characterized with energy-dispersive X-ray (EDX) spectroscopy and electron backscatter diffraction (EBSD). Changes in austenite:ferrite galvanic activity caused by the applied thermal treatment were investigated by measuring the Volta-Potential difference of the two phases using scanning Kelvin probe force microscopy (SKPFM) [14,15]. Measurements showed that the two phases reached closer surface potential values in the HAZ. The passivation behaviour of the individual phases in the wrought alloy and the simulated HAZ was also investigated, using electrochemical potentio-dynamic polarization in an H_2SO_4/HCl electrolyte [16,17]. The aim of this work is to identify the effect of welding on the galvanic activity between austenite and ferrite in the HAZ. The observations on the galvanic behaviour changes are used to expand the knowledge of the electrochemical behaviour of the dual phase alloy in the HAZ of the weld.

2. Experimental methodology

The wrought material used was a solution annealed DSS grade 2205 (UNS S1803) in the form of a pipe (38 mm wall thickness) with chemical composition (in %wt.) of 22.0Cr, 5.1Ni, 2.48Mo, 1.77 Mn, 0.022C, 0.16 N and Fe (bal). Cylindrical samples (100 mm length and 10 mm diameter) were extracted longitudinally from the pipe wall, by

* Corresponding author at: Corrosion and Protection Centre, Room D26, Jackson's Mill Building, University of Manchester, Sackville St. Campus, Manchester, M13 9PL, UK.
E-mail addresses: pierfranco.reccagni@postgrad.manchester.ac.uk (P. Reccagni), d.engelberg@manchester.ac.uk (D.L. Engelberg).

https://doi.org/10.1016/j.corsci.2019.108198
Received 2 March 2019; Received in revised form 21 August 2019; Accepted 2 September 2019
Available online 04 September 2019

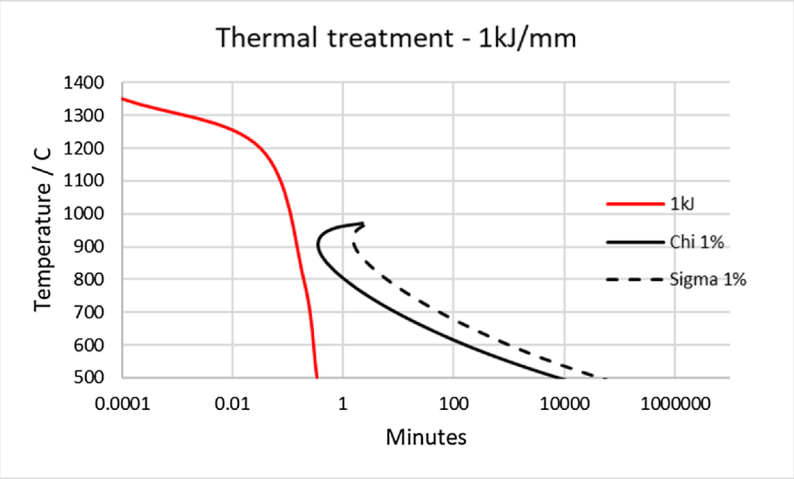

Fig. 1. Thermal history of the simulated HAZ (red) with 1% Sigma and Chi theoretical CCT curves.

EDM cutting, and a thermal treatment to produce a simulated HAZ was applied using a Gleeble 3500 thermo-mechanical simulator.

The thermo-mechanical simulation was designed to replicate the HAZ of a single-pass TIG weld performed using a welding heat input (HI) of 1.0 kJ/mm. The thermal history is described as a sequence of heating and cooling intervals; a definition of relationship between the temperature intervals and cooling times can be found in [18], where a similar approach was used to study the DSS microstructure in the HAZ. The correlation of the thermal history with the welding HI is determined using empirical nomograms, which considers also the thickness of the welded piece [19]. The simulation was performed by heating the sample to 1350 °C for 2 s followed by controlled cooling; the cooling intervals were 2 s in the 1350 °C–1200 °C range, 11.5 s in the 1200 °C -800 °C interval and 20 s between 800 °C -500 °C. The cooling rate was selected with the purpose to avoid formation of sigma and chi phases, for which CCT curves were produced using JMatPro®. The CCT curves and the thermal history applied to the sample are shown in Fig. 1. The thermal treatment was performed in air.

The wrought material (i.e. as-received base metal, BM) and the material subjected to thermal simulation (i.e. the gleeble simulated HAZ) were cut into 10 mm diameter coupons and mounted in conductive epoxy resin. After wet-grinding to 2400 grit, diamond paste polishing to 1 µm and colloidal silica finishing (20–40 nm, 30 min), the microstructure was characterized by EBSD. Maps with a typical dimension of 1.0 mm × 0.8 mm were acquired using 600 nm step size in a FEI Quanta 650 FEG-SEM equipped with a Nordlys EBSD detector from Oxford Instruments. The data were processed using HKL Channel 5 software from the same manufacturer. EDX data for local chemical compositions were acquired using X-Max detector of 80 mm^2, collecting 10^6 counts for each point. EDX spectra were quantified using Aztec software for ZAF correction. In the wrought material (AR), 5 spectra were acquired for each phase. In the simulated HAZ, where the chemical composition shows larger local variations, 30 spectra were collected.

The same surface preparation was used for Volta-Potential surveys. After the preparation, samples were kept for 2 days at ambient temperature and humidity, without applying any passivation treatment. Measurements were performed in a Dimension D3100 AFM, using platinum-coated tips (OSCM-PT) with 25 nm tip radius. Measurements were performed in amplitude modulation with 50 nm scan lift height and maps were acquired over 80 µm × 80 µm regions at 0.2 kHz scan frequency, acquiring 512 lines per scan and 512 points per line, giving a theoretical resolution of approximatively 150 nm per pixel. Measurements were performed at room temperature and humidity.

The same materials (i.e. the wrought alloy and the simulated HAZ) were used for electrochemical measurements. The surfaces were prepared by wet grinding to a 1200 grit finish followed by cleaning in ethanol and de-ionized water. A custom-built three-electrode miniature set-up was used in a micro-cell, as described elsewhere [20], with an exposed circular region of 1.5 mm diameter (1.77mm^2 area) and a solution volume in the cell of 3 ml. All measurements were performed at room temperature using an Ag/AgCl/3.0 M KCl reference electrode and a Ivium Compactstat.e potentiostat. The electrolyte used was 2 M H_2SO_4 + 0.5 M HCl [21] and the scan rate used was 0.1 mV/s.

3. Results

3.1. Microstructure

Phase maps of the BM and the Gleeble simulated HAZ

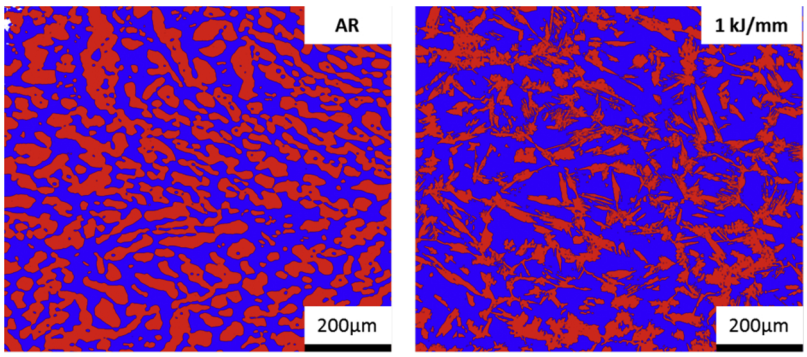

Fig. 2. EBSD phase maps of base metal (a) and simulated HAZ (b). austenite in red, ferrite in blue.

Table 1
Chemical compositions of the phases in the wrought metal and simulated HAZ (EDX ZAF corrected).

Element/ PREN formula	Average EDX analyses, normalised wt% (SD)					
	Wrought metal			Simulated HAZ		
	Ferrite	Austenite	Difference between phases	Ferrite	Austenite	Difference between phases
Cr	**24.1** (< 0.1)	**21.1** (< 0.1)	**3**	**22.7** (0.6)	**21.3** (0.6)	**1.4**
Mo	**3.7** (< 0.1)	**1.8** (< 0.1)	**1.9**	**3.5** (0.2)	**2.7** (0.2)	**0.8**
Ni	**4.2** (< 0.1)	**6.7** (< 0.1)	**2.5**	**4.9** (0.4)	**6.2** (0.4)	**1.2**
Mn	**1.6** (< 0.1)	**1.8** (< 0.1)	**0.2**	**1.6** (0.1)	**1.7** (0.1)	**0.1**

SD = standard deviation.

microstructures are shown in Fig. 2. The austenite:ferrite ratio in the BM sample was 51:49 while in the simulated HAZ sample the austenite content was reduced and the phase ratio was 38:62. EBSD analysis was applied to investigate both microstructures, but no further crystallographic phases were found (e.g. sigma, chi).

An expected consequence of the thermal treatment is the change in chemical composition of austenite and ferrite. While isothermal annealing enables redistribution of austenite and ferrite-forming elements to the respective favoured phases via diffusion, the fast cooling cycle in the HAZ inhibits this re-distribution. The differences in Cr, Mo, Ni and Mn contents between the austenite and ferrite became far smaller in the Gleeble simulated microstructure, compared to the wrought base material. EDX spectra acquired in different grains of the simulated HAZ also show larger composition variations in each phase, which is reflected in larger standard deviations (SD) summarized in Table 1. Of particular interest is also the change in Cr and Mo concentrations between the BM material and the gleeble simulated microstructure; the ferrite became depleted in both elements in the simulated HAZ, with Cr reduced by 1.4% and Mo by 0.2%, whereas the HAZ austenite showed higher contents of both elements.

3.2. SKPFM measurements

Volta potential (Ψ) measurements were used to investigate the change in galvanic activity between austenite and ferrite on a local scale. A SKPFM map of the BM material was compared to four maps from different locations of the simulated HAZ. A set of typical maps is given in Fig. 3, where line scans measuring the Volta-potential difference between austenite and ferrite ($\Delta\Psi^{\gamma:\delta}$) are shown.

In order to avoid effects of the different austenite:ferrite ratios on the measured potential difference in the two microstructures, the potential has been measured within the individual phases using the average value of 10 μm long line scans. An example of these measurements can be seen in Fig. 3. Line-scan measurements showed a great variation across different positions within individual phases, reflected in the standard deviation (SD) of the average values. Measurements were acquired for each map in five different positions for both austenite and ferrite. While austenite in both conditions showed consistently cathodic character with respect to ferrite, the average austenite-ferrite Volta potential difference was found to be reduced in the simulated HAZ. The average difference found in the wrought BM sample was 47 mV, while an average value of 24 mV was measured in the four maps acquired from the HAZ. The results of the austenite-ferrite Volta potential difference on the simulated HAZ have been normalized with respect to the difference in the wrought BM microstructure, and the decreased galvanic activity expressed as fraction of the value of the wrought BM material. Results of all SKPFM measurements are summarized in Table 2.

The measurements showed consistently that the potential contrast between the two phases was reduced in the simulated HAZ, showing a potential difference of approximately 50% of that measured in the wrought BM microstructure.

3.3. Polarization test in H_2SO_4 + HCl

Polarization scans were initially performed over a wide potential range in order to identify the location of the austenite and ferrite activation peaks. Scans were then carried out over a narrower potential range, focusing on the activation peaks only. The final potential range selected was ranging from −50 mV vs. OCP to −100 mV vs. Ag/AgCl, with typical scans shown in Fig. 4.

The activation peaks for austenite and ferrite were clearly separated and easy to identify for the wrought BM sample. In the simulated HAZ, the observed activation peaks of both phases were all overlapping. The activation curves for the austenite were partially hidden behind the more dominant ferrite peak, with the two phases not completely resolved in these polarization scans. While the activation peaks for austenite in the HAZ were not fully evident, both times the polarization curves showed a change of trend in the region corresponding to the austenite activation seen in the BM microstructure.

In order to highlight the austenite contribution in the activation curve for the HAZ, a Gaussian deconvolution of the peaks has been performed, as shown in Fig. 5. Reasonable fitting of the activation curve was possible, resulting in two separated activation peaks accounting for the austenite dissolution.

The difference between austenite and ferrite passivation potential was 80 mV in the wrought/base metal, while this difference reduced to 60 mV in the simulated HAZ. Despite this variation in passivation behaviour of the two phases, in both measurements the free corrosion potential was found to be unchanged (−285 mV) with or without the applied heat treatment. Another difference observed was the difference in relative current contribution of austenite and ferrite to the global activation current. Integration of the polarization curve in the activation region showed similar values of charge for the alloy components oxidation for both materials of ≈50 μC. However, while in the wrought BM 76% of the charge was provided by the ferrite and 24% from the austenite, in the simulated HAZ ferrite dissolution contributed for 92% of the total activation current, while the austenite contribution was reduced to 8%. Two factors are likely to have caused this change in the simulated HAZ. In first place, the ferrite fraction in this microstructure is higher: 62% in the simulated HAZ compared to 49% in the wrought base metal. Secondly, the differences in the Cr and Mo contents of the two phases is reduced compared with respect to the wrought base metal, potentially causing changes in the electrochemical passivation reactions.

4. Discussion

DSS welds show high susceptibility to EAC in the HAZ. One of the most noticeable consequences of the welding process on this region is the reduction of austenite content. EAC resistance of DSSs is greatly affected by the phase ratio, with values approaching the ideal 50:50

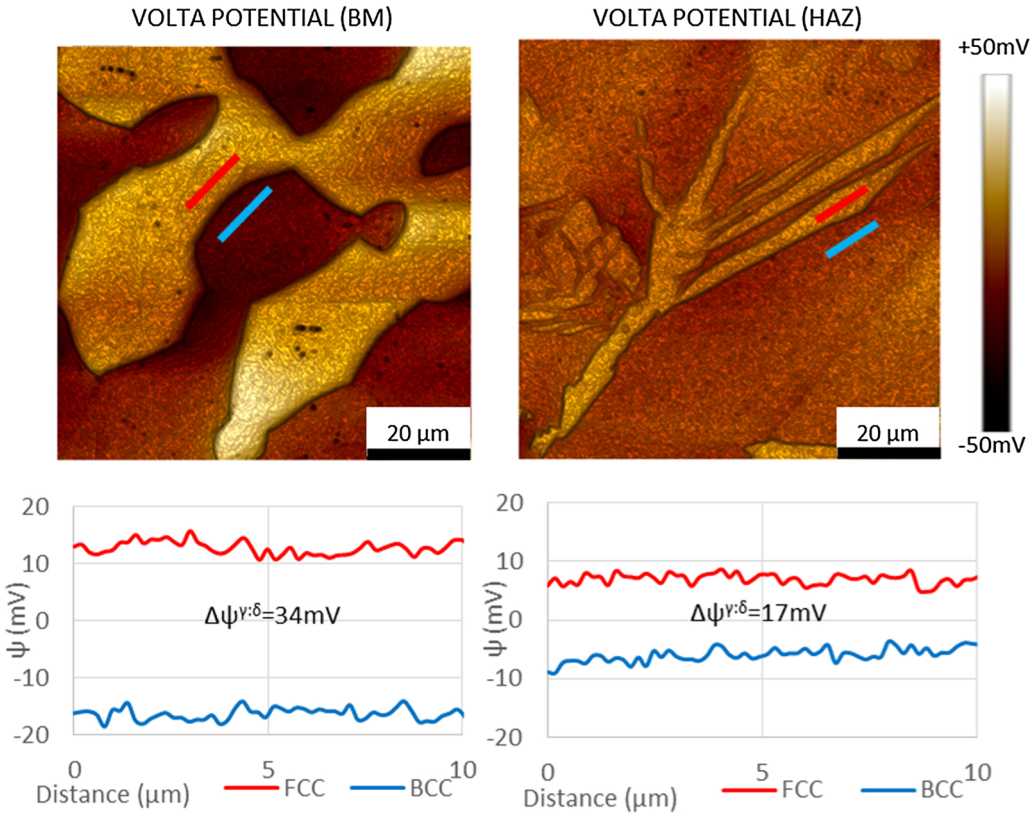

Fig. 3. SKPFM measurements on the wrought metal/base metal (BM) (left) and the simulated HAZ (right) with a corresponding heat input of 1.0 kJ/mm. From top to bottom: height map, Volta-Potential map, example of line scans in FCC-austenite (red) and BCC-ferrite (blue).

Table 2
Summary of the SKPFM Volta-Potential measurements.

$\Delta\psi^{\gamma:\delta}$		$\frac{\Delta\psi^{\gamma:\delta}_{HAZ}}{\Delta\psi^{\gamma:\delta}_{BM}} x100$
Base Metal	Simulated HAZ	
47 (SD 4.4) mV	24 (SD 2.3) mV	51 %
	26 (SD 3.5) mV	55 %
	22 (SD 4.1) mV	47 %
	24 (SD 2.1) mV	51 %

distribution showing the best performance [22]. The thermal treatment experienced in the HAZ caused several alterations in the alloy microstructure. Even when acceptable phase balance is achieved, the chemical composition for austenite and ferrite in the HAZ shows great variation with respect to individual phase composition in the wrought alloys in the annealed state.

Within the HAZ, partitioning of the austenite and ferrite-forming elements between the phases is reduced compared to the wrought base metal, due to the initial transformation to ferrite of the microstructure and the relative fast cooling that allows diffusion of heavy elements only over a short distance (i.e. a few microns) [23]. As a result, the chemical compositions of the austenite and the ferrite become more similar, with a marked reduction of chromium content in the latter.

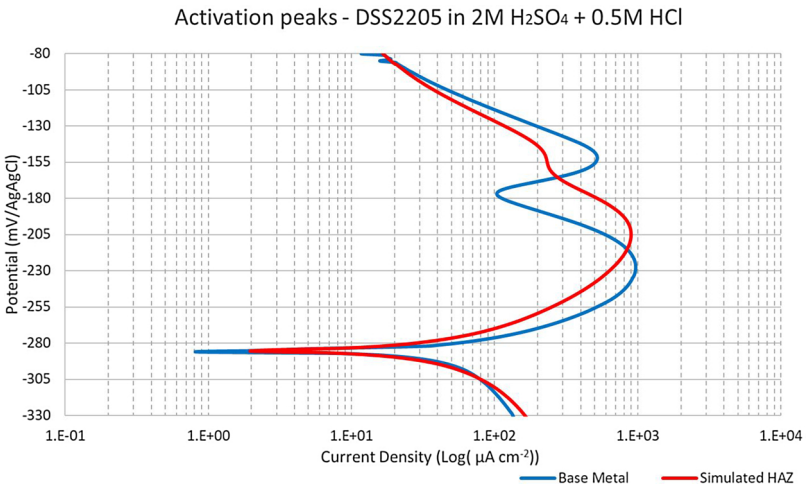

Fig. 4. PTD polarization curves in the activation region. Wrought/base metal in blue, simulated HAZ in red.

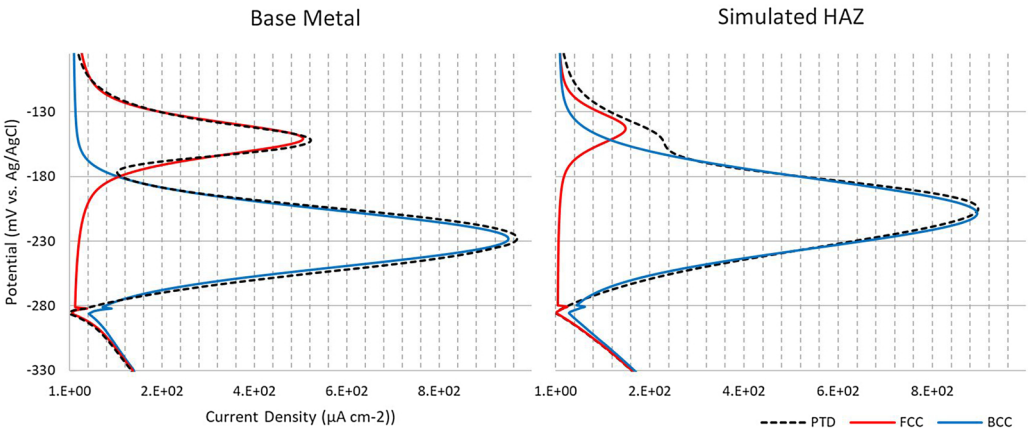

Fig. 5. Deconvolution of the PTD polarization curves in the activation regions for the wrought/base metal (left) and the simulated HAZ (right). FCC-austenite activation curves in red, BCC-ferrite in blue.

Similar findings have been reported by [24], who also correlated the chromium depletion of the ferrite with enhanced localised corrosion susceptibility in this phase.

The effect of the galvanic coupling between austenite and ferrite is already visible in the formation of the passive film on the grade 2205surface. Studies on the passivation behaviour of the individual constituent phases in near-neutral chlorides containing solutions showed that the passive current density required to sustain the passive film on each phase is higher than the current density required for the duplex microstructure when both phases are coupled [25,26]. The fraction of Cr_2O_3 in the passive films formed on austenite and ferrite phases is higher in the duplex alloy, while significant fractions of Cr $(OH)_3$ were found on the constituent phases passivated individually. Chromium hydroxides in the passive film cause lower corrosion resistance (i.e. efficiency of the passive film), explaining the higher corrosion resistance of the film formed when both phases are coupled [25,26].

The different corrosion properties of austenite and ferrite are of paramount importance for the outstanding EAC resistance of DSSs. In modern grades, in which austenite is present in the form of dispersed islands and ferrite is the continuous phase, in chloride-containing environments localised corrosion and EAC initiates in the latter, with cracks often propagating along phase boundaries. The ability of austenite to stop the crack progression relies on its higher corrosion potential, with short crack nuclei observed in the austenite phase [26]. When a crack in ferrite reaches an austenite island, the anodic activity at the crack tip is reduced by the difference in potential/pH conditions required for austenite to corrode [22]. The different condition required for austenite corrosion forces the crack to stop, unless ductile tearing via mechanical overload or other forms of embrittlement of the austenite occurs. For this protection mechanism to work, a difference in chemical composition, resulting in different corrosion potentials for the two phases is needed.

While the change in ferrite composition and its higher susceptibility to localised corrosion can explain the increased likelihood of crack nucleation sites in this phase, clarifying the relation with EAC susceptibility requires an understanding of changes in the global electrochemical properties of the thermally altered alloy (i.e. the simulated HAZ in the current study). In particular, the evolution of austenite and ferrite relative nobility could give an indication on the mechanism behind the reduced EAC resistance of the HAZ. The SKPFM measurements and the electrochemical polarization in chloride-containing environments constitute two different ways to investigate the quality and the formation of the passive film on austenite and ferrite in the different microstructures.

The Volta-potential difference highlights the relative nobility of the austenite-ferrite native passive films. The passivation of the alloys in this case occurs in air, once the polishing is completed, and the potential measured relates to the native passive film. These observations reveal the localised passive film nobility and show the Volta-Potential difference of austenite and ferrite as an intrinsic property of the two phases. These measurements are not influenced by the different phase ratios in the wrought base metal and in the HAZ, and they are independent from the austenite morphology and distribution. As a result, the reduction in Volta-potential difference of the phases in the HAZ is a direct consequence of the different chemical composition of the two phases after the thermal cycle applied by the welding process.

Potentio-dynamic polarization was used to understand the consequences of these changes on the global electrochemical behaviour of the alloy. When using the mixture of sulphuric and hydrochloric acid, the difference in electrochemical nobility between austenite and ferrite results in the existence of two distinct anodic peaks in the active-to-passive region of the polarization curve, with the austenite activation potential being higher than that of ferrite. In the simulated HAZ, this effect is reduced, due to the similar chemical composition of the two phases upon the thermal gleeble treatment. With the increased ferrite content, the activation peak for this phase occupies a larger area of the active-to-passive region in the potentiodynamic curve. As a result, the austenite activation peak is hidden and deconvolution is needed to identify it. The electrochemical potential difference between the phases (i.e. activation peaks) is smaller in the HAZ, confirming that the reduction in relative nobility of the two phases is determined by the different passivation mechanism of the microstructure in the two conditions.

The activation peaks have been studied in terms of electrochemical potential, an intrinsic property determined by the chemical composition. The electric charge associated with the ferrite peak in the HAZ, however, was found much larger (92% of the total activation current) than in the base metal (76%). The larger variation in the chemical composition of both phases in the HAZ would ultimately result in larger potential variations and associated current responses around to the mean. This would explain the broader current peaks and larger charge of the ferrite, with however lower overall measured current density.

The work in this paper contributes to the understanding of the effect of weld microstructure electrochemical behaviour in the HAZ on the corrosion behaviour and EAC susceptibility of duplex stainless steels. The results clearly show a marked effect of the thermal history on the internal galvanic activity of duplex stainless steel weld microstructure. Implications of this finding have been discussed in the frame of EAC microstructure resistance. The use of a simulated HAZ was preferred over a real-scale weld, allowing for a more thermally controlled microstructure to be generated. The same techniques can also be used to assess real weld microstructures, with characterization of the corrosion behaviour and internal galvanic activity in different regions of lean

duplex stainless steel multi-pass welds reported elsewhere [27].

5. Conclusions

The galvanic activity between austenite and ferrite has been investigated using samples prepared from wrought 2205 DSS base metal in the solution annealed condition and an HAZ, simulated in the same material using a Gleeble thermo-mechanical simulator. The simulated HAZ was designed to correspond to that of a single pass TIG weld. The following conclusions can be drawn:

- The Gleeble-simulated microstructure shows a significant reduction in volta-potential difference between austenite and ferrite compared to similar measurements on the base metal;
- Polarization measurements conducted in H_2SO_4/HCl electrolyte showed that the simulated weld HAZ thermal cycle affects the alloy passivation behaviour, reducing the difference in activation potentials between the two phases in the HAZ;
- The chemical partitioning, caused by the simulated welding thermal cycle, reduced the galvanic activity between the two phases in the HAZ with potential effects on the EAC resistance of the DSS.

Acknowledgments

This work was financially supported through an i-case EPSRC PhD studentship and TWI (The Welding Institute, Cambridge). The authors express their gratitude to Dr. Vahid A. Hosseini for the ThermoCalc® calculations of the CCT curves.

References

[1] R.N. Gunn, Developments, grades and specifications, Duplex Stainl. Steel. Microstruture, Prop. Appl. (1997), pp. 1–13, https://doi.org/10.1533/9781845698775.1.
[2] W.-T. Tsai, M.-S. Chen, Stress corrosion cracking behavior of 2205 duplex stainless steel in concentrated NaCl solution, Corros. Sci. 42 (2000) 545–559, https://doi.org/10.1016/S0010-938X(99)00105-5.
[3] C. Örnek, F. Léonard, S.A. Mcdonald, Time-dependent in situ measurement of atmospheric corrosion rates of duplex stainless steel wires, Npj Mater. Degrad. (2018), https://doi.org/10.1038/s41529-018-0030-9.
[4] R.N. Gunn, Microstructure, Duplex Stainl. Steels, Woodhead Publishing Limited, 1997, pp. 24–49, https://doi.org/10.1533/9781845698775.24.
[5] Z. Zhang, H. Jing, L. Xu, Y. Han, L. Zhao, J. Zhang, Influence of microstructure and elemental partitioning on pitting corrosion resistance of duplex stainless steel welding joints, Appl. Surf. Sci. 394 (2017) 297–314, https://doi.org/10.1016/j.apsusc.2016.10.047.
[6] S. Atamert, J.E. King, Elemental partitioning and microstructural development in duplex stainless steel weld metal, Acta Metall. Mater. 39 (1991) 273–285, https://doi.org/10.1016/0956-7151(91)90306-L.
[7] R.C. Newman, Stress corrosion cracking, Shreir's Corros. (2010) 864–901, https://doi.org/10.1016/B978-044452787-5.00035-4.
[8] S. Edition, Metallurgy second edition welding metallurgy, Structure 822 (2003) 466, https://doi.org/10.1016/j.theochem.2007.07.017.
[9] R.N. Gunn, Welding metallurgy, Duplex Stainl. Steels, (1997), pp. 110–132, https://doi.org/10.1533/9781845698775.110 w, Abington, England.
[10] V.A. Hosseini, L. Karlsson, C. Örnek, P. Reccagni, S. Wessman, D. Engelberg, Microstructure and functionality of a uniquely graded super duplex stainless steel designed by a novel arc heat treatment method, Mater. Charact. 139 (2018), https://doi.org/10.1016/j.matchar.2018.03.024.
[11] W.-T. Tsai, S.-L. Chou, Environmentally assisted cracking behavior of duplex stainless steel in concentrated sodium chloride solution, Corros. Sci. 42 (2000) 1741–1762, https://doi.org/10.1016/S0010-938X(00)00029-9.
[12] BS-EN-ISO, Specification and Qualification of Welding Procedures for Metallic Materials — Welding Procedure Test —, (2012), pp. 1–32.
[13] H.Y. Liou, R.I. Hsieh, W.T. Tsai, Microstructure and pitting corrosion in simulated heat-affected zones of duplex stainless steels, Mater. Chem. Phys. 74 (2002) 33–42, https://doi.org/10.1016/S0254-0584(01)00409-6.
[14] C. Örnek, D.L. Engelberg, Correlative EBSD and SKPFM characterisation of microstructure development to assist determination of corrosion propensity in grade 2205 duplex stainless steel, J. Mater. Sci. (2015), https://doi.org/10.1007/s10853-015-9501-3.
[15] Y. Guo, T. Sun, J. Hu, Y. Jiang, L. Jiang, J. Li, Microstructure evolution and pitting corrosion resistance of the Gleeble-simulated heat-affected zone of a newly developed lean duplex stainless steel 2002, J. Alloys. Compd. 658 (2016) 1031–1040, https://doi.org/10.1016/j.jallcom.2015.10.218.
[16] I.H. Lo, Y. Fu, C.J. Lin, W.T. Tsai, Effect of electrolyte composition on the active-to-passive transition behavior of 2205 duplex stainless steel in H2SO4/HCl solutions, Corros. Sci. 48 (2006) 696–708, https://doi.org/10.1016/j.corsci.2005.02.004.
[17] W.T. Tsai, J.R. Chen, Galvanic corrosion between the constituent phases in duplex stainless steel, Corros. Sci. 49 (2007) 3659–3668, https://doi.org/10.1016/j.corsci.2007.03.035.
[18] H.-Y. Liou, R.-I. Hsieh, W.-T. Tsai, Microstructure and stress corrosion cracking in simulated heat-affected zones of duplex stainless steels, Corros. Sci. 44 (2002) 2841–2856, https://doi.org/10.1016/S0010-938X(02)00068-9.
[19] R.-I. Hsieh, H.-Y. Liou, Y.-T. Pan, Effects of cooling time and alloying elements on the microstructure of the gleeble-simulated heat-affected zone of 22% Cr duplex stainless steels, J. Mater. Eng. Perform. 10 (2001) 526–536, https://doi.org/10.1361/105994901770344665.
[20] L. Guilherme, A. Benedetti, C. Fugivara, A portable electrochemical microcell for weld inspection of duplex stainless steel tanks, Corrosion (2018) 3004, https://doi.org/10.5006/3004.
[21] S. Aoki, H. Yakuwa, K. Mitsuhashi, J. Sakai, Dissolution behaviour of alpha and gamma phases of a duplex stainless steel in a simulated crevice solution, ECS Trans. 25 (2010) 17–22.
[22] R.A. Cottis, R.C. Newman, Stress Corrosion Cracking Resistance of Duplex Stainless Steels, Health and Safety Executive - Offshore Technology Report, (1993).
[23] A.J. Ramirez, The relationship between chromium nitride and secondary \nAustenite precipitation in duplex stainless steels, Metall. Mater. Trans. A 34A (2003) 1575–1597.
[24] C.M. Garzón, C.A. Serna, S.D. Brandi, A.J. Ramirez, The relationship between atomic partitioning and corrosion resistance in the weld-heat affected zone microstructures of UNS S32304 duplex stainless steel, J. Mater. Sci. 42 (2007) 9021–9029, https://doi.org/10.1007/s10853-007-1881-6.
[25] X. Cheng, Y. Wang, C. Dong, X. Li, The beneficial galvanic effect of the constituent phases in 2205 duplex stainless steel on the passive films formed in a 3.5% NaCl solution, Corros. Sci. 134 (2018) 122–130, https://doi.org/10.1016/j.corsci.2018.02.033.
[26] X. Cheng, Y. Wang, X. Li, C. Dong, Interaction between austenite-ferrite phases on passive performance of 2205 duplex stainless steel, J. Mater. Sci. Technol. 34 (2018) 2140–2148, https://doi.org/10.1016/j.jmst.2018.02.020.
[27] D.L. Guihlerme, L.H. Reccagni, P. Benedetti, A.V. Fugivara, C.S. Engelberg, Corrosion assessment of ASME qualified welding procedures for grade 2101 lean duplex stainless steel, Corrosion (2019), https://doi.org/10.5006/3257.